

MULTI-SCALE COMPONENT-TREES FOR ENHANCED REPRESENTATION IN MULTIPLEX IMMUNOHISTOCHEMISTRY IMAGING

Romain Perrin¹, Aurélie Leborgne¹, Nicolas Passat², Benoît Naegel¹, Cédric Wemmert¹

¹ ICube, University of Strasbourg, France

² Université de Reims Champagne Ardenne, CReSTIC, Reims, France

ABSTRACT

Multiplex immunohistochemistry (mIHC) is an innovative method that simultaneously labels multiple biomarkers in the same tissue section with different colored stains. However, analyzing these complex images is a challenging task for current image processing methods. In order to efficiently process these images, it may be beneficial to employ an effective representation of the data. The component-tree is known to facilitate the representation of images containing sparse objects, which necessitate representation at a higher scale, as opposed to large background regions that can be represented at a lower scale without loss of fidelity. In this paper, we present how a multi-scale version of the component-tree can be effectively utilized to represent this type of data, drawing inspiration from the approach a pathologist might take when analyzing these images (initially identifying objects of interest via a specific nuclear channel, such as DAPI, and then associating each object with a spectral signature based on the intensities of other channels). We demonstrate this method on an unsupervised analysis of 9-channel multiplexed glioblastoma data.

Index Terms— Multiplex immunohistochemistry images, Component-tree, Multi-scale.

1. INTRODUCTION

Multiplex imaging is a development in histopathology that allows for the identification of diverse cell types within a singular image, marking a substantial progression beyond the conventional histopathological approaches limited to two immunohistochemical markers. This technological advancement unveils a sophisticated spatial analysis of cellular interactions, thereby enriching the comprehension of the intrinsic biological mechanisms. However, it is not without challenges, as issues such as image quality, and the availability and accuracy of annotations, remain critical in the precise identification, segmentation, and classification of cellular structures. Indeed, in dense tissues, cells may overlap in the z -dimension, making it difficult to identify individual cells. The variety of cell types and shapes, along with the reliance on expert-annotated data for machine learning algorithms, introduces even more complexities.

In the context of multiplex imaging data, segmentation predominantly employs machine learning algorithms, including user-guided pipelines such as CellProfiler [1], and more recently, deep learning algorithms, mainly convolutional neural networks like DeepCell [2], U-Net [3], or CellPose [4]. These algorithms, however, hinge on training utilizing manually annotated data (ground truth) by expert users. This reliance introduces potential challenges such as annotation bias and interobserver variability, which may influence cell segmentation outcomes. The absence of a universally accepted gold

standard in the field, coupled with a dependency on expert experience [5], underscores the complexities and challenges intrinsic to multiplex image analysis.

To address the issue of annotation availability and quality in this type of images, we propose an unsupervised approach based on the use of a multi-spectral multi-scale component-tree. Our idea is to emulate the approach of human pathologists who rely on the DAPI (dihydrochloride) channel to initially identify cells because it roughly reveals nuclear area according to their DNA density. Then, they explore other channels for specific markers to identify more precisely their phenotype.

Our methodology relies on the use of the component-tree (or max-tree) [6], a morphological graph-based model known for its efficient image encoding and low computational complexity [7].

Component-trees have been involved in various areas of image processing, for example in nuclear imaging: PET [8, 9, 10], PET/MRI [11], PET/CT [12, 13, 14, 15], in brain MRI [16], in angiographic imaging [17, 18, 19, 20, 21], in microscopy [22, 23, 24], in dermatology [25], or for visualization purposes [26], and even recently into self-supervised deep learning tasks [27].

More precisely, we aim in this work at augmenting the component-tree model by integrating multi-scale and multi-spectral information from various image channels during its construction process. Primarily, a first multi-scale component-tree is constructed on the DAPI channel, which inherently contains essential objects of interest such as cell nuclei, while concurrently encapsulating information from auxiliary channels within each node.

Secondly, multi-spectral characteristics gathered from the various image channels are integrated into the tree, allowing to improve the classification of objects. Our goal is to contribute to a better understanding of cellular interactions and biological mechanisms in the context of multiplex histopathological images.

2. MATERIAL AND METHODS

2.1. Data and annotations

To validate our approach, we used data from a collaborative project on glioblastoma, with neuropathologists from the Hannover Medical School. Glioblastoma (GBM) is a malignant brain tumor with poor prognosis despite aggressive treatment. The biological behavior of cells at their invasive edge is of major importance for clinical course and patients' quality of life.

Data We obtained 63 multiplex histochemistry images from 22 patients to analyze. These images were acquired by the following protocol. Formalin-Fixed Paraffin-Embedded tissue was cut into 3 μ m thick sections and stained for DAPI, GFAP, ATRX, IDH1, MS4A4A, CD68, CD206, CD3 and CD34. Whole slides were scanned with

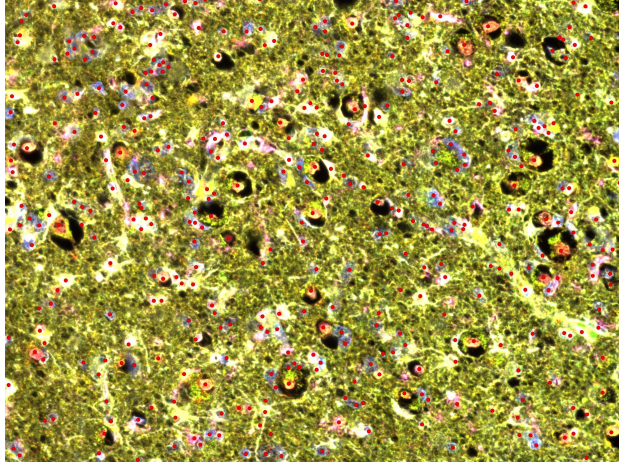


Fig. 1: Example of annotated image, where each red disk indicates a cell of interest.

a $20\times$ magnification at a resolution of $0.49\text{ }\mu\text{m/pixel}$ (Vectra Polaris, Akoya Biosciences). In these, we manually selected regions ranging from tumor core to adjacent normal tissue, avoiding artifacts like folds, noise, or tissue border effects. These regions were multispectral acquired at a resolution of $0.25\text{ }\mu\text{m/pixel}$ (Vectra Polaris, Akoya Biosciences) and color deconvoluted with prerecorded spectral libraries for all Opal fluorophores using Inform 2.6 (Akoya Biosciences), resulting in multi-channel (a channel corresponds to a single fluorophore/marker, see Table 1 for more details) TIFF format images of 1860×1396 pixels.

Annotations Point annotations were provided by different pathologists on the images. Each cell of interest was marked by at least three pathologists, and results were consolidated when disagreements were noted. See Figure 1.

2.2. Multispectral, multiscale component-tree

Component-tree The component-tree (or max-tree) [6] encodes the inclusion relations between the connected components of the successive threshold sets of a grayscale image.

More formally, let $f : \mathbb{Z}^2 \rightarrow V$ be a grayscale 2D image, with $V \subset \mathbb{N}$. For any nonempty subset $X \subseteq \mathbb{Z}^2$, we note $CC(X)$ the set of the connected components of X . The upper threshold set of f at a value $\lambda \in V$ is denoted as $[f \geq \lambda] = \{x \in \mathbb{Z}^2 \mid f(x) \geq \lambda\}$.

The component-tree (or max-tree) of f is defined as the Hasse diagram of the partially ordered set $(\bigcup_{\lambda \in V} CC([f \geq \lambda]), \subseteq)$. Its root (i.e. its maximum) is the set \mathbb{Z}^2 , which is the unique connected component of $[f \geq 0]$. Its leaves (i.e. its minimal elements) are the flat zones of locally maximal value in the image. An example of component-tree is illustrated in Figure 2.

Multiscale component-tree In [28], we have proposed a multiscale extension of the component-tree, namely the Multi-Scale Component-Tree (MSCT), enabling to encode in an unique hierarchical structure various objects from different levels of resolution. The main purpose is to represent background and/or non-relevant parts of the image within flat zones at the lowest scales, while representing relevant / fine detailed parts of the image within flat zones at the highest scales. We only recall here the main steps of

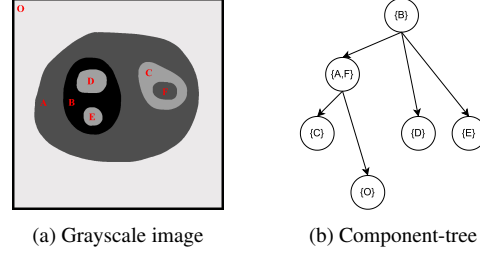


Fig. 2: The component-tree (b) of a grayscale image (a). Individual nodes correspond to connected components at specific gray levels, while links between nodes represents the inclusion relations between the corresponding flat zones.

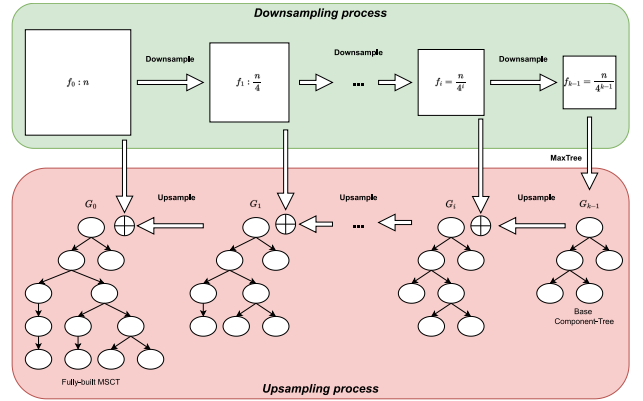


Fig. 3: Illustration of the MSCT construction.

the MSCT construction: first, the initial image is downsampled at various scales, then an initial component-tree is computed from the lowest scale. Second, following an iterative scheme, each significant region (i.e. node) is promoted from one scale to the next, enabling to refine it (i.e. improve its resolution). A new component-tree for this region is then computed at the next scale and grafted onto the initial tree. The construction process of the MSCT is illustrated in Figure 3.

Multispectral and multiscale component-tree The MSCT has been defined on grayscale images. In this work we propose to use the MSCT in the context of multispectral images. A 2D multispectral image with k channels can be denoted as a function $f : \mathbb{Z}^2 \rightarrow V^k$.

The MSCT is built on the DAPI channel following the construction steps described in [28] with the following modifications. Before the first downsampling operation, a contrast enhancement step is performed to better account for lowly-contrasted flat zones that would otherwise not be considered during the later scale upsampling and segmentation operations. Contrast limited adaptive histogram enhancement (CLAHE) [29] is thus applied to the DAPI channel.

Nuclei segmentation from the MSCT Once the MSCT is fully-enriched, a set of nodes is extracted by minimizing a stability criterion based on the concept of maximally stable extremal regions (MSER) as described in [28].

On this fully-enriched MSCT, a set of nodes of interest N can be chosen using the same selection method integrated with the scale enrichment steps. These nodes' flat zones may contain several nuclei

Table 1: Characteristics of each deconvoluted channel.

	DAPI	GFAP	MS4A4A	CD3	IDH1	CD206	ATRX	CD68	CD34
Name (Opal)		480	520	540	570	620	650	690	780
Emission (nm)	461	500	525	536	570	616	650	694	770

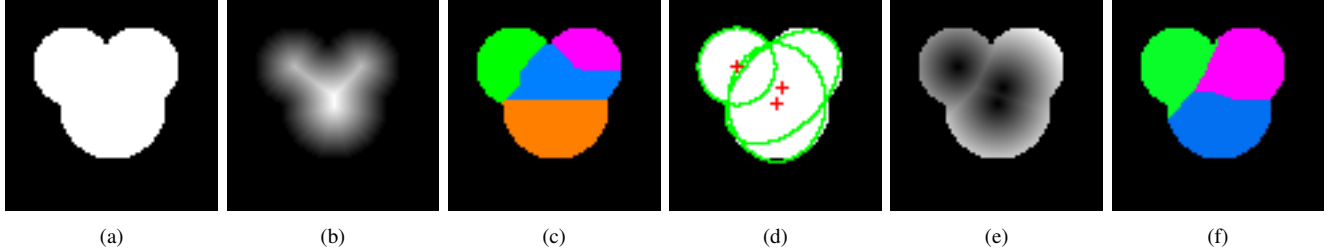


Fig. 4: (a) Illustration of overlapping nuclei. (b) Application of the classic Euclidean distance transform to the nuclei. (c) Resulting watershed segmentation derived from the maximum intensity peaks of the Euclidean distance transform. (d) Distance Transform Ellipse Center Method Algorithm (DTECMA). (e) Distance transform to the nearest ellipse center as obtained from DTECMA. (f) Watershed segmentation resulting from the DTECMA approach.

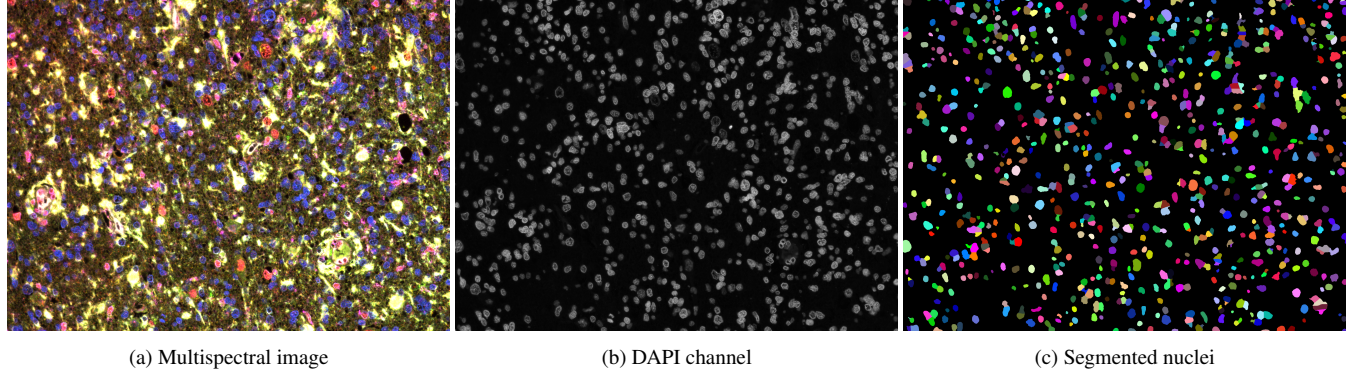


Fig. 5: (a) A multispectral image, (b) its DAPI channel on which the MSCT is computed and (c) the resulting segmented nuclei.

as these objects could touch or overlap each other.

For each flat zone $n_i \in N$, the number of underlying nuclei is estimated by the mean of an ellipse fitting model as nuclei tend to exhibit elliptical shapes. The Distance Transform-based Ellipse-Contour Matching Algorithm (DTECMA) [30] is used to estimate the number of ellipses and their respective centers across each flat zone. Ellipse centers too close to each other are merged together and the center of mass of all merged ellipses' centers is taken as the newly-merged ellipse center.

These ellipse centers are then used to initialize flooding basins in a watershed algorithm. The classic Euclidean distance transform cannot be used as the ellipse centers do not necessarily match the local peaks in such transform. A new distance transform is defined on a set of ellipse centers E_{n_i} and a connected component CC_{n_i} . The new distance transform is defined as:

$$d_c(p) = \min \{ \|p - e\|_2 \mid e \in E_{n_i}, p \in CC_{n_i} \} \quad (1)$$

This distance transform assigns to each pixel the distance to its closest ellipse center, guaranteeing that the ellipse centers are among its local maxima. The addition of DTECMA and the new distance transform is able to better separate clusters formed by highly-overlapping nuclei as illustrated in Figure 4.

The resulting partitions of n_i form the final segmented nuclei S in the form of connected components.

On each of the segmented nuclei $s_i \in S$, features can be computed to qualify the underlying object. Here, we make use of the other channels, each of which is associated with a specific biomarker by considering s_i as a mask across all channels f^i of the multispectral image. Let f by a multispectral image containing k channels. f^i is the i^{th} channel of f and $f^i(p)$ is the value of a pixel p in the i^{th} channel. A feature vector c_i is computed for s_i by summing the pixel values in each channel for all pixels belonging to the mask:

$$c_i = \left[\sum_p f^j(p) \mid p \in n_i \right]_{j=1}^k \quad (2)$$

3. RESULTS

Segmentation evaluation A total number of $n = 62$ ($1396 \times 1860 \times 9$) multispectral images have been processed out of the 63 available. One image has been removed from the computation as it did not exhibit the sparsity of nuclei present in the rest of the dataset and would not benefit from the parameters set for the dataset. The following parameters have been used:

- Number of scales: 3 (from $\frac{1}{1}$ scale for the base component-tree to $\frac{1}{16}$ scale for the nodes upsampled after the last construction step).
- δ parameter for the MSER stability computation: 10% of the MSCT tree height.
- Maximum MSER stability for nodes during the upsampling step: 1.0.
- Maximum pixel area allowed for nodes at the upsampling step: 0.20% of image size (5 193 pixels).
- Maximum MSER stability for nodes during the segmentation step (tree filtering): 1.0.
- Maximum pixel area allowed for nodes at the segmentation step: 0.15% of image size (3 895 pixels).
- Minimum pixel area for single nuclei to remove artifacts: 100 pixels.

An example of such multispectral image, its DAPI channel and the resulting application of the MSCT segmentation is illustrated in Figure 5.

A total number of 24 296 punctual annotations with labels are used to evaluate the quality of the obtained segmentation.

Across $n = 62$ images, there has been total number of 18 494 true positive nuclei, 6 457 false positive nuclei and 5 802 false negative nuclei for a precision of 0.741 and a recall of 0.761.

Discussion By looking at small regions within the images such as those illustrated in Figure 6, we can assess the quality of the resulting segmentation by noticing its inherent ability to preserve the contours of extracted objects. This property is inherited from the component-tree serving as base structure for the MSCT.

We can also point out that, despite the addition of local contrast enhancement in the form of CLAHE [29], even sizable objects fail to be properly segmented if segmented at all due to their lower than average contrast to the background. This is especially visible in Figure 6(c,d) when looking at the central nucleus or in Figure 6(e,f) when looking at the top right nucleus. A further improvement could consist of adding a preprocessing step in the form of thresholding the lowest part of the DAPI signal prior to the local contrast enhancement, allowing it to be used with higher settings.

Lastly, there is a high proportion of false positives across this dataset. The main reason to why this behavior exists is the very nature of the DAPI marker. There are regions across the images containing a higher than average contrast to the background yet these regions do not seem to be associated with any underlying nuclei. This could probably not be easily fixed by altering the signal in a preprocessing step as for the previous issue.

4. CONCLUSION

In this paper, we proposed an extension to the newly-defined concept of Multi-Scale Component-Tree (MSCT), a multi-scale and hierarchical representation of an image. We proposed to represent multispectral images and more specifically multiplex immunohistochemistry images as the sparse nature of nuclei would benefit from the MSCT representation. We have built the MSCT on the channel containing a nucleus biomarker (DAPI) and showed its ability to accurately segment nuclei by using the inherent hierarchical representation of said MSCT and no supervision. Feature vectors carrying the multispectral information contained in the other channels have been defined and aggregated in the nodes of the MSCT. These vectors provide a signature for every segmented nucleus and could be further used to carry out classification tasks.

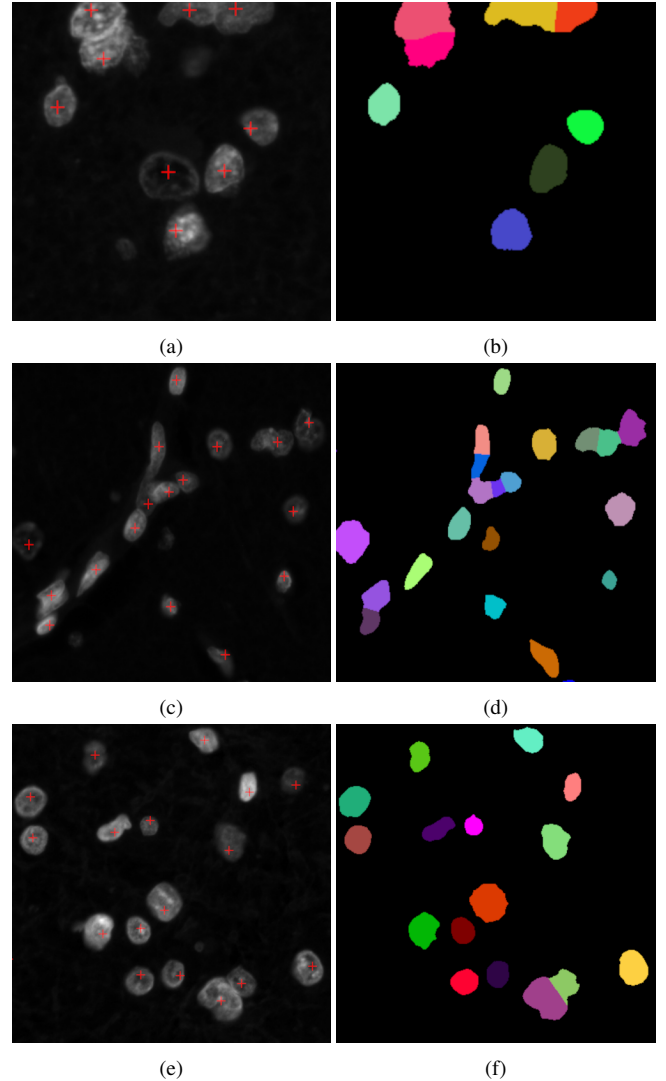


Fig. 6: Examples of DAPI channel with superimposed punctual annotations (a,c,e) and corresponding MSCT segmentation (b,d,f).

5. COMPLIANCE WITH ETHICAL STANDARDS

This research study was conducted retrospectively using human subject data from a collaborative project on glioblastoma, with neuropathologists from the Hannover Medical School. This study was performed in line with the principles of the Declaration of Helsinki.

6. ACKNOWLEDGEMENTS AND CONFLICTS OF INTERESTS

This work was funded by ArtIC project “Artificial Intelligence for Care” (grant ANR-20-THIA-0006-01) and co-funded by Région Grand Est, Inria Nancy - Grand Est, IHU of Strasbourg, University of Strasbourg and University of Haute-Alsace and by the 3rd Joint Transnational Call for European Research Projects on Systems Medicine Mi*EDGE project (grant ANR-19-SYME-0004-03). The authors have no financial or non-financial interests to disclose.

7. REFERENCES

- [1] A E Carpenter, T R Jones, M R Lamprecht, C Clarke, I H Kang, O Friman, D A Guertin, J H Chang, R A Lindquist, J Moffat, P Golland, and D M Sabatini, “Cellprofiler: image analysis software for identifying and quantifying cell phenotypes,” *Genome Biology*, vol. 7, pp. R100, 2006.
- [2] D Bannon, E Moen, M Schwartz, E Borba, T Kudo, N Greenwald, V Vijayakumar, B Chang, E Pao, E Osterman, W Graf, and D Van Valen, “Deepcell kiosk: scaling deep learning-enabled cellular image analysis with kubernetes,” *Nature Methods*, vol. 18, pp. 43–45, 2021.
- [3] T Falk, D Mai, R Bensch, Ö Çiçek, A Abdulkadir, Y Marrakchi, A Böhm, J Deubner, Z Jäckel, K Seiwald, A Dovzhenko, O Tietz, C Dal Bosco, S Walsh, D Saltukoglu, T Leng Tay, M Prinz, K Palme, M Simons, I Diester, Brox T, and O Ronneberger, “U-Net: deep learning for cell counting, detection, and morphometry,” *Nature Methods*, vol. 16, pp. 67–70, 2019.
- [4] C Stringer, T Wang, M Michaelos, and M Pachitariu, “Cellpose: a generalist algorithm for cellular segmentation,” *Nature Methods*, vol. 18, pp. 100–106, 2021.
- [5] D Segebarth, M Griebel, N Stein, C R von Collenberg, C Martin, D Fiedler, L B Comeras, A Sah, V Schoeffler, T Lüffe, A Dürr, R Gupta, M Sasi, C Lillesaar, M D Lange, R O Tasan, N Singewald, H-C Pape, C M Flath, and R Blum, “On the objectivity, reliability, and validity of deep learning enabled bioimage analyses,” *Elife*, vol. 9, pp. e59780, 2020.
- [6] P Salembier, A Oliveras, and L Garrido, “Anti-extensive connected operators for image and sequence processing,” *IEEE Transactions on Image Processing*, vol. 7, pp. 555–570, 1998.
- [7] E Carlinet and T Géraud, “A comparative review of component tree computation algorithms,” *IEEE Transactions on Image Processing*, vol. 23, pp. 3885–3895, 2014.
- [8] É Grossiord, H Talbot, N Passat, M Meignan, P Tervé, and L Najman, “Hierarchies and shape-space for PET image segmentation,” in *ISBI*, 2015, pp. 1118–1121.
- [9] H Urien, I Buvat, N Rougon, M Soussan, and I Bloch, “Brain lesion detection in 3D PET images using max-trees and a new spatial context criterion,” in *ISMM*, 2017, pp. 455–466.
- [10] É Grossiord, N Passat, H Talbot, B Naegel, S Kanoun, I Tal, P Tervé, S Ken, O Casasnovas, M Meignan, and L Najman, “Shaping for PET image analysis,” *Pattern Recognition Letters*, vol. 131, pp. 307–313, 2020.
- [11] H Urien, I Buvat, N Rougon, S Boughdad, and I Bloch, “3D PET-driven multi-phase segmentation of meningiomas in MRI,” in *ISBI*, 2016, pp. 407–410.
- [12] É Grossiord, H Talbot, N Passat, M Meignan, and L Najman, “Automated 3D lymphoma lesion segmentation from PET/CT characteristics,” in *ISBI*, 2017, pp. 174–178.
- [13] D L Farfan Cabrera, N Gogin, D Morland, B Naegel, D Papathanassiou, and N Passat, “Segmentation of axillary and supraclavicular tumoral lymph nodes in PET/CT: A hybrid CNN/component-tree approach,” in *ICPR*, 2020, pp. 6672–6679.
- [14] D L Farfan Cabrera, É Grossiord, N Gogin, D Papathanassiou, and N Passat, “Analysis of lymph node tumor features in PET/CT for segmentation,” in *ISBI*, 2021, pp. 588–592.
- [15] F J Alvarez Padilla, B Romaniuk, B Naegel, S Servagi-Vernat, D Morland, D Papathanassiou, and N Passat, “Hierarchical forest attributes for multimodal tumor segmentation on FDG-PET/contrast-enhanced CT,” in *ISBI*, 2018, pp. 163–167.
- [16] P Dokládal, I Bloch, M Couprie, D Ruijters, R Urtasun, and L Garnero, “Topologically controlled segmentation of 3D magnetic resonance images of the head by using morphological operators,” *Pattern Recognition*, vol. 36, pp. 2463–2478, 2003.
- [17] M H F Wilkinson and M A Westenberg, “Shape preserving filament enhancement filtering,” in *MICCAI*, 2001, pp. 770–777.
- [18] B Caldaírou, N Passat, and B Naegel, “Attribute-filtering and knowledge extraction for vessel segmentation,” in *ISVC*, 2010, pp. 13–22.
- [19] A Dufour, N Passat, B Naegel, and J Baruthio, “Interactive 3D brain vessel segmentation from an example,” in *ISBI*, 2011, pp. 1121–1124.
- [20] A Dufour, B Naegel, C Ronse, J Baruthion, V Wolff, and N Passat, “From 2D markers in MIP to 3D vessel segmentation: A fuzzy paradigm for connected filtering,” in *ISBI*, 2013, pp. 922–925.
- [21] A Dufour, O Tankyevych, B Naegel, H Talbot, C Ronse, J Baruthio, P Dokládal, and N Passat, “Filtering and segmentation of 3D angiographic data: Advances based on mathematical morphology,” *Medical Image Analysis*, vol. 17, pp. 147–164, 2013.
- [22] D Sariöz, T Y Kong, and G T Herman, “History trees as descriptors of macromolecular structures,” in *ISVC*, 2006, pp. 263–272.
- [23] R R Snapp, E Goveia, L Peet, N A Bouffard, G J Badger, and H M Langevin, “Spatial organization of fibroblast nuclear chromocenters: component tree analysis,” *Journal of Anatomy*, vol. 223, pp. 255–261, 2013.
- [24] C Meyer, É Baudrier, P Schultz, and B Naegel, “Combining max-tree and CNN for segmentation of cellular FIB-SEM images,” in *RRPR, Selected Papers*, 2022, pp. 77–90.
- [25] B Naegel, N Passat, N Boch, and M Kocher, “Segmentation using vector-attribute filters: methodology and application to dermatological imaging,” in *ISMM*, 2007, pp. 239–250.
- [26] M A Westenberg, J B T M Roerdink, and M H F Wilkinson, “Volumetric attribute filtering and interactive visualization using the max-tree representation,” *IEEE Transactions on Image Processing*, vol. 16, pp. 2943–2952, 2007.
- [27] Q Tang, B Du, and Y Xu, “Self-supervised learning based on max-tree representation for medical image segmentation,” in *IJCNN*, 2022, pp. 1–6.
- [28] R Perrin, A Leborgne, N Passat, B Naegel, and C Wemmert, “Multi-scale component-tree: A hierarchical representation for sparse objects,” in *DGMM*, 2024.
- [29] K Zuiderveld, “Contrast limited adaptive histogram equalization,” in *Graphics Gems IV*, p. 474–485. Academic Press Professional, Inc., USA, 1994.
- [30] T Zou, T Pan, M Taylor, and H Stern, “Recognition of overlapping elliptical objects in a binary image,” *Pattern Analysis and Applications*, vol. 24, pp. 1193–1206, 2021.